Sub-Nano Pt/β-FeOOH Quantum Dots for Photocatalytic Removal of Toluene: Catalyst Design, Preparation, and Benefits

Mengxi Pei[1], Shangchun Lv[1], Yishui Liu[1], Zhichun Si[1]*, Xiaodong Wu[2], Rui Ran[2], Duan Weng[1] and Feiyu Kang[2]

[1]Shenzhen International Graduate School, Tsinghua University, Shenzhen, China, [2]School of Materials, Tsinghua University, Beijing, China

Photocatalytic removal of organic pollutants under solar irradiation at room temperature is considered an energy-saving technique of environmental remediation. However, photocatalysis is impeded by the poor response to visible light and fast charge recombination. In this work, sub-nano Pt/β-FeOOH quantum dots (QDs) were designed to shorten the charge migration path and obtain wide light harvesting. Interestingly, the crystalline β-FeOOH QDs can be obtained by loading sub-nano Pt particles *via* a reconstruction mechanism of amorphous FeOOH induced by H_2 spillover, which facilitates the fast kinetics of charge transition and benefits the oxygen-rich surface of the catalyst for photocatalytic oxidation reactions. Moreover, the Pt-V_O-Fe interfaces were proved to be the most active sites for the activation of O_2. As a result, the catalyst exhibits a predominant photocatalytic performance in toluene oxidation, achieving a TOF_{Pt} of 0.591 min^{-1} at room temperature under visible light irradiation. This work provides a new perspective on the design and preparation of nanocatalysts for high-efficient photocatalysis under visible light irradiation.

Keywords: β-FeOOH QD, sub-nano Pt, recrystallization, photocatalysis, toluene oxidation

INTRODUCTION

Solar-based photocatalysis under ambient conditions is regarded as an effective and energy-saving method for the removal of volatile organic compounds (VOCs) (Guo et al., 2021). Electrons and holes will be generated if the semiconductor photocatalysts are irradiated by light with energy higher than the semiconductor's bandgap and then will react with O_2, H_2O, or hydroxyl groups to form highly active radicals to degrade the VOC molecules (Mateo et al., 2021). However, semiconductor-based photocatalysts suffer from the low utilization rate of visible light due to their wide bandgap and fast charge recombination. Numerous methods have been exploited to solve these problems, such as doping/loading metals (Asahi et al., 2001; Kang et al., 2020), constructing 2D morphologies (Wang et al., 2018), and heterojunctions (Zhong et al., 2021). But all these methods have their own shortcomings, for example, it is difficult to synthesize good interfaces for high-efficient heterojunctions; and doping may lead to more bulk defects as recombination centers of electrons and holes (Mamaghani et al., 2017; Schreck and Niederberger, 2019; Han et al., 2021). They still lack an efficient and universal method to construct high-efficient photocatalysts.
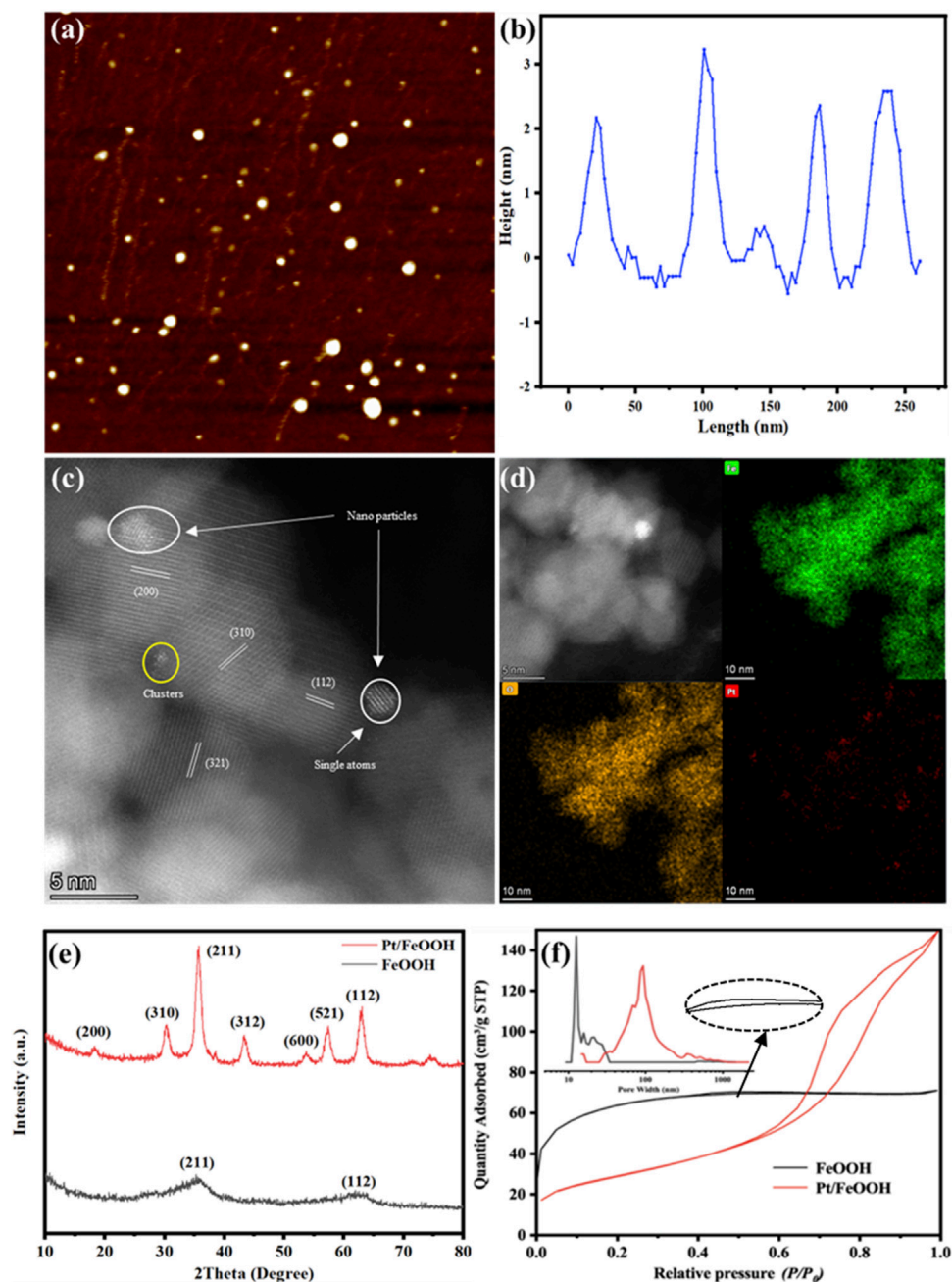
FIGURE 1 | (A) AFM image of FeOOH QDs. **(B)** Height distribution curves of FeOOH QDs. **(C)** AC STEM photos of Pt/FeOOH. **(D)** EDS photos and elemental mapping of Pt/FeOOH. **(E)** X-ray diffraction patterns of samples. **(F)** Nitrogen adsorption/desorption isotherms and the corresponding pore size distribution curves (inset).

Generally, catalysts with small sizes tend to exhibit better catalytic performances than large particles, owing to more active sites on their surfaces. 2D materials have been synthesized and used for obtaining more surface active sites and shortening the charge diffusion path, such as graphene (Gurbani et al., 2018), g-C₃N₄ (Hosseini et al., 2018), and hydrotalcite (Dong et al., 2021). Furthermore, 2D quantum dots (QDs) are 0D nanomaterials whose all the three spatial dimensional scales

(<10 nm) are within the nanoscale range, which always possess distinctive properties, for example, the quantum confinement and high surface-to-volume ratios with more active edge sites per unit mass (Jouyandeh et al., 2021). However, the crystalline structure of QDs may be difficult to be maintained and leads to the amorphous features with large defects, which may act as the recombination centers for electrons and holes. In this work, our strategy was: first, FeOOH QDs

TABLE 1 | BET surface area, pore diameters, and pore volumes of samples.

Sample	d_{pore} (nm)	V_{pore} (cm³/g)	S_{BET} (m²/g)
FeOOH	12.7	0.11	209.3
Pt/FeOOH	93.1	0.23	104.6

(bandgap of 2.02 eV), which have wide light absorption from UV to visible light, were synthesized to shorten the charge diffusion paths; second, sub-nano Pt particles were loaded on the surface of FeOOH QDs to act as the active sites for toluene oxidation. Interestingly, the amorphous FeOOH QDs were crystalized during the loading process of Pt, but the QD parameters were maintained. The benefit of this consequence keeps that the charge separation efficiency of the catalyst was greatly improved. On the other hand, the photocatalyst has a mismatching time scale in photocatalysis. It has been reported that the most important step of toluene oxidation is the activation of oxygen molecules (Pal et al., 2012; Sakamoto et al., 2015; Niklas et al., 2018; Huang et al., 2020; Mi et al., 2021). But the time scale of surface reactions is nanosecond, which is much slower than that of charge generation (femtosecond) and diffusion (picosecond) (Qian et al., 2019). Therefore, we not only designed the reducible Fe^{2+}/Fe^{3+} pairs to ensure the support could activate oxygen but also enhanced the surface reaction process through loading platinum. In addition, it is reported that platinum can work as active site for active small molecules and produce LSPR-based photocatalysis (Einaga et al., 2001; Marsh et al., 2004; Yuan et al., 2014; Chen et al., 2017). The results of this research indicated that the enhancement in light absorbance of FeOOH by sub-nano Pt particles was negligible, but the improvement in oxygen activation played an important role. Therefore, the reconstruction of amorphous $Fe(OH)_3$ to crystalline β-FeOOH during the loading process of Pt species is discussed in detail, and its benefit for oxygen activation and the consequent photocatalytic activity in toluene oxidation are highlighted.

RESULTS AND DISCUSSION

Morphology and Textural Property

Atomic force microscopy (AFM) and scanning transmission electron microscopy (STEM) are carried out to investigate the morphologies of FeOOH QDs and Pt particles. From the images in **Figure 1A–C**, the FeOOH QDs are in the size of 5 nm with an average height of 3–3.5 nm. From **Figure 1C**, various aggregations of Pt atoms can be found, such as nanoparticles (2 nm), clusters (0.6 nm), and single atomic Pt. The EDS elemental mapping in **Figure 1D** proves this result.

Figure 1E displays the XRD patterns of FeOOH and Pt/FeOOH. The diffraction peaks of Pt/FeOOH located at 18.2°, 30.3°, 35.7°, 43.3°, 53.7°, 57.4°, and 63.0° are assigned to (200), (310), (211), (321), (600), (521), and (112) facets of β-FeOOH (JCPDS NO. 34-1266) (Liu et al., 2017; Yang et al., 2018). It should be noted that the peak intensities of Pt/FeOOH are obviously higher than those of FeOOH, indicating that the crystalline structure of FeOOH QD was greatly improved after

loading Pt *via* reconstruction. No diffraction peaks of Pt species can be detected due to the low content and high dispersion of Pt.

The specific surface area and pore size distribution curves of FeOOH and Pt/FeOOH were analyzed on the basis of N_2 sorption isotherms, and the results are shown in **Figure 1E, F** and **Table 1**. As shown in **Figure 1F**, the adsorption/desorption isotherms of FeOOH are type I curves that show a mesoporous property. For Pt/FeOOH, the adsorption/desorption isotherms can be classified as type IV curves and H3 hysteresis loops in a wide relative pressure region, indicating the co-existence of mesopores and macropores (Fu et al., 2013). The mean pore sizes of FeOOH and Pt/FeOOH are 12.7 and 93.1 nm, respectively. The difference is that FeOOH has a more obvious adsorption/desorption platform, which means that the catalyst has a more regular pore size, while Pt/FeOOH has disordered pore size distribution. The evolutions of pores and surface area of FeOOH after loading Pt prove the reconstruction of FeOOH QD in the synthesis process. **Figure 2** shows the synthesis mechanism of Pt/FeOOH QD.

Structure Evolution of FeOOH QDs Induced by the Metal–Support Interaction

The metal–support interaction–induced reconstructions of metals in reactions are extensively reported (Duan et al., 2018; Hu et al., 2019; van Deelen et al., 2019). The support works not only to disperse the NPs but also to influence the catalytic activity of the catalyst by affecting the stability, morphology, and electronic structure of the metals. However, how to prepare a good photocatalyst *via* a metal–support interaction during the synthesis process has seldom been reported. Generally, β phase FeOOH can be obtained using ferric chloride as starting material (Song and Boily, 2012; Liu et al., 2016). Moreover, only amorphous FeOOH QDs were reported to be synthesized at room temperature (Song and Boily, 2012; Liu et al., 2016; Song and Boily, 2016). Similarly, defect-rich FeOOH QDs were also prepared in this work, as indicated by the amorphous characteristic XRD signals and SAED images in **Supplementary Figure S2**. Unfortunately, the amorphous phase usually has too many oxygen vacancies which will induce serious charge recombination in photocatalysis. In order to obtain well-crystallized photocatalysts, high-temperature treatment is always needed, which will lead to the crystal growth or serious segregation of QDs. Interestingly, in this work, loading Pt species using $NaBH_4$ as a reduction agent led to the crystallization of amorphous FeOOH QDs at room temperature, which can avoid the crystal growth during high-temperature treatment.

FeOOH QDs occur as nanoparticles and are covered by hydroxyl functional groups coordinated to one (-OH), two (m-OH), or three (m3-OH) underlying iron atoms. Goethite (α-FeOOH) is a high thermodynamic stable phase, while lepidocrocite (γ-FeOOH) and akaganéite (β-FeOOH) are metastable phases. β-FeOOH has a 2 × 2 channel structure containing chloride ions stabilized by H-bonds of variable strength. β-FeOOH QDs have positive surface energies which are in favor of the metastable phases and restrain the phase transformation to a more stable goethite. The topotactic
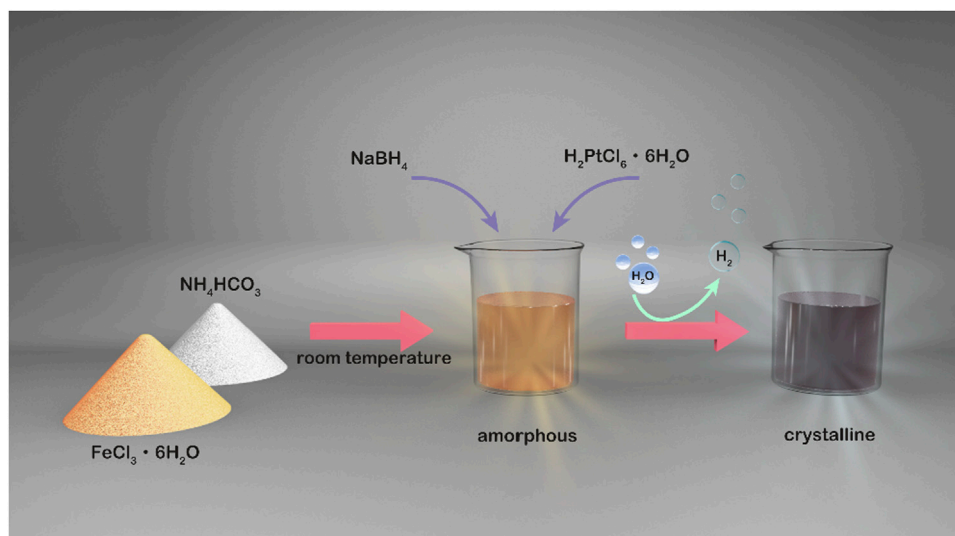
FIGURE 2 | Synthesis mechanism of Pt/FeOOH QD.
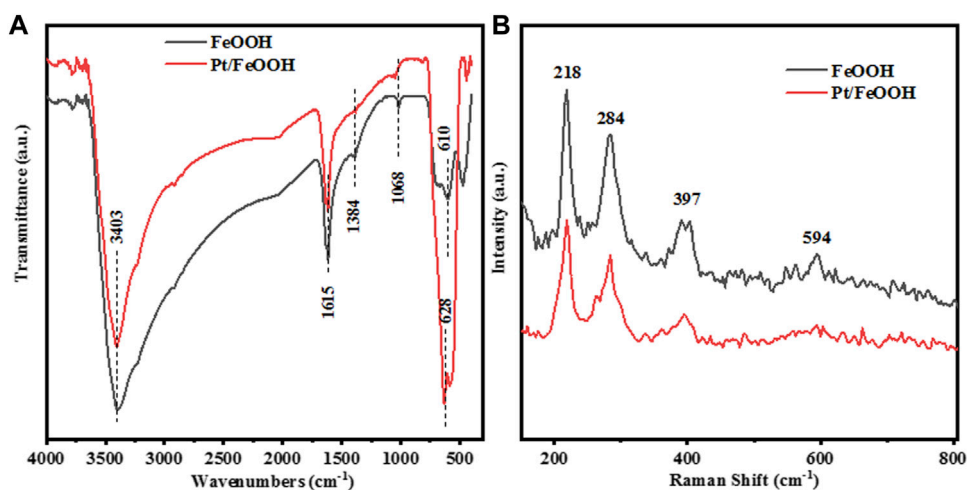
FIGURE 3 | (A) FT-IR spectra and **(B)** Raman spectra of samples.

transformations among iron oxyhydroxides are kinetically controlled *via* the migration and release of H_2O, resulting from the association of adjacent (hydrogen-bonded) OH groups (Song and Boily, 2016). This route was verified by FTIR, Raman, XPS, and XANES/EXAFS spectra in this work.

The FTIR spectra of FeOOH and Pt/FeOOH are shown in **Figure 3A**. The broadband centered at 3,403 cm^{-1} is assigned to the stretching vibration of the hydrogen-bonded hydroxyl groups. The prominent peak at around 600–650 cm^{-1} can be ascribed to the asymmetric stretching vibration of Fe-O-Fe (Song and Boily, 2016). The loading of Pt species using $NaBH_4$ as a reduction agent led to significant decreases in peak intensity of hydroxyls and increases in Fe-O-Fe species, indicating the release of H_2O in this process. Moreover, the band at 628 cm^{-1} of Pt/

FeOOH shows an obvious peak splitting, indicating crystallization of FeOOH. When Pt particles formed on the surface of FeOOH QDs, more hydrogen molecules may adsorb on the Pt metals and spill over to the surface of FeOOH and react with hydroxyl groups to release H_2O. Therefore, Pt metals help in the removal of H_2O and benefit the crystallization of FeOOH. The change in another prominent peak at 1615 cm^{-1}, attributing to the adsorbed water species, also consolidates the same mechanism. Raman spectra of FeOOH and Pt/FeOOH are displayed in **Figure 3B**. The bands at 218, 294, and 397 cm^{-1} can be attributed to asymmetric stretching of metal-hydroxide groups, and an active peak that appears at 594 cm^{-1} can be assigned to the vibration of hydroxyl groups connected to the structural defect sites (Liu et al., 2013; Peng et al., 2021). The
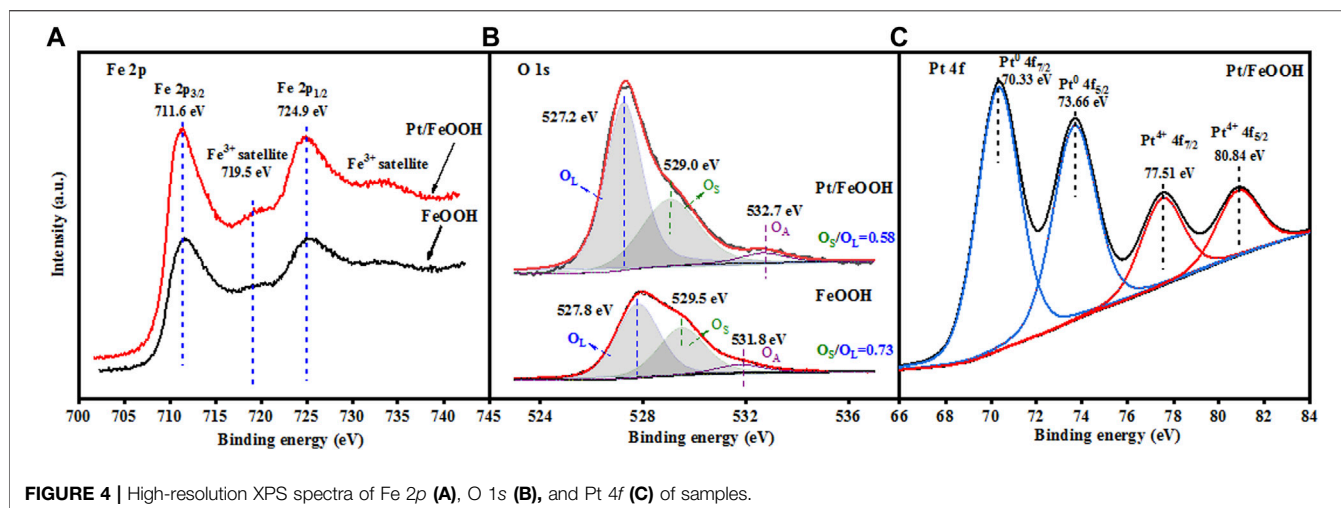
FIGURE 4 | High-resolution XPS spectra of Fe 2*p* **(A)**, O 1*s* **(B),** and Pt 4*f* **(C)** of samples.

TABLE 2 | Surface compositions of samples.

Sample	Real loading of Pt (wt%)	Surface Pt^0/Pt^{4+} ratio	Surface O_S/O_L molar ratio	Total oxygen peak area
FeOOH	-	-	0.73	16593
Pt/FeOOH	0.23	3:1	0.58	31951

crystallization of FeOOH QDs leads to the removal of oxygen vacancies and hydroxyl groups, resulting in the attenuation of these Raman bands.

The XPS spectrum displayed in **Figure 4** is to analyze the surface compositions and chemical states of elementals on FeOOH and Pt/FeOOH. The calculated results are listed in **Table 2**.

The high-resolution XPS peaks of Fe 2*p* (**Figure 4A**) for FeOOH and Pt/FeOOH are centered at 711.6, 724.9, and 719.5 eV, which show negligible shifts but distinct increases in the peak intensity of Fe^{3+} (Peng et al., 2021), also suggesting the better crystallinity of Pt/FeOOH than FeOOH. The binding energies of Pt $4f_{5/2}$ and Pt $4f_{7/2}$ are at 70.33/73.66 eV and 77.51/80.84 eV (**Figure 4B**), attributing to the Pt^0 and Pt^{4+} species, respectively (Peng et al., 2021). The band area of Pt^{4+} and Pt^0 in Pt/FeOOH is close to 1:3 (**Table 2**), suggesting that Pt^{4+} may be on the interfaces due to the close contact of FeOOH and Pt species. Also, part of the Pt^{4+} peak can be attributed to the unreduced $PtCl_6^{2-}$ species during preparation. The high-resolution XPS peaks of O 1*s* (**Figure 4C**) for FeOOH and Pt/FeOOH can be divided into three peaks, including lattice oxygen (O_L, at 527.8 and 527.2 eV), surface oxygen species including OH, O^-, and O^{2-} (O_S, 529.5, and 529.0 eV), and adsorbed H_2O and/or intercalated carbonate and carbon dioxide (O_A, 531.8Pt-V_O-Fe and 532.7 eV), respectively. It is noticeable that remarkable redshifts of the binding energies of oxygen species on Pt/FeOOH are compared with those on FeOOH, 0.6 eV for O_L and 0.5 eV for O_S, suggesting that electron transfer occurred from Pt to lattice oxygen and surface oxygen species which results in the formation of oxidized interface Pt^{4+} species. The ratio of O_S/

O_L for Pt/FeOOH (0.58) remains lower than that for FeOOH (0.73) due to the good crystallization of the former. Meanwhile, the peak area of total oxygen species for Pt/FeOOH (31951) is much larger than that of FeOOH (16593), indicating that all oxygen species are increased obviously after the deposition of Pt, especially for the lattice oxygen.

The local coordination chemistry of the Fe atoms in the catalyst was probed by X-ray absorption near the edge structure (XANES) and the extended X-ray absorption fine structure (EXAFS). As is shown in **Figure 5A**, the XANES spectra manifest that the valence state of Fe in the FeOOH and Pt/FeOOH samples is similar to that in the Fe_2O_3 reference. In addition, the absorption edge for Pt-FeOOH redshifts was compared with that of FeOOH, indicating fewer defects in Pt/FeOOH. Moreover, the amplitude of the Fe K-edge oscillation for Pt/FeOOH is significantly increased, suggesting the good crystallization of FeOOH (**Figure 5B**). **Figure 5C** shows the R space plots for both samples. The first Fe-O shell of FeOOH is at ~ 1.98 Å, attributing to a coordination number (N) of 5.8 (Sadykov et al., 2021), which indicates many oxygen vacancies in the matrix of crystal. As for Pt/FeOOH, the first Fe-O shell peak appears at ~ 1.94 Å, corresponding to a coordination number (N) of 6.0 (**Table 3**) (Sadykov et al., 2021), which is nearly the theoretical value of an octahedral structure. These results verified the good crystalline nature of Pt/FeOOH and the Pt-O-Fe interfaces. Moreover, the shortened Fe-O bond and elongated Fe-Fe bond in Pt/FeOOH compared with those of FeOOH consolidate the Pt-O-Fe-rich interfaces. We tried to probe the local coordination chemistry of Pt atoms; unfortunately, the XAS

FIGURE 5 | Normalized XANES spectra **(A),** Fourier-transformed k^2-weighted of the Fe K-edge EXAFS spectra in R-space **(B),** and Fe K-edge EXAFS oscillation function $k^2 \chi(k)$ in K-space **(C)** of FeOOH (black) and Pt/FeOOH (red).
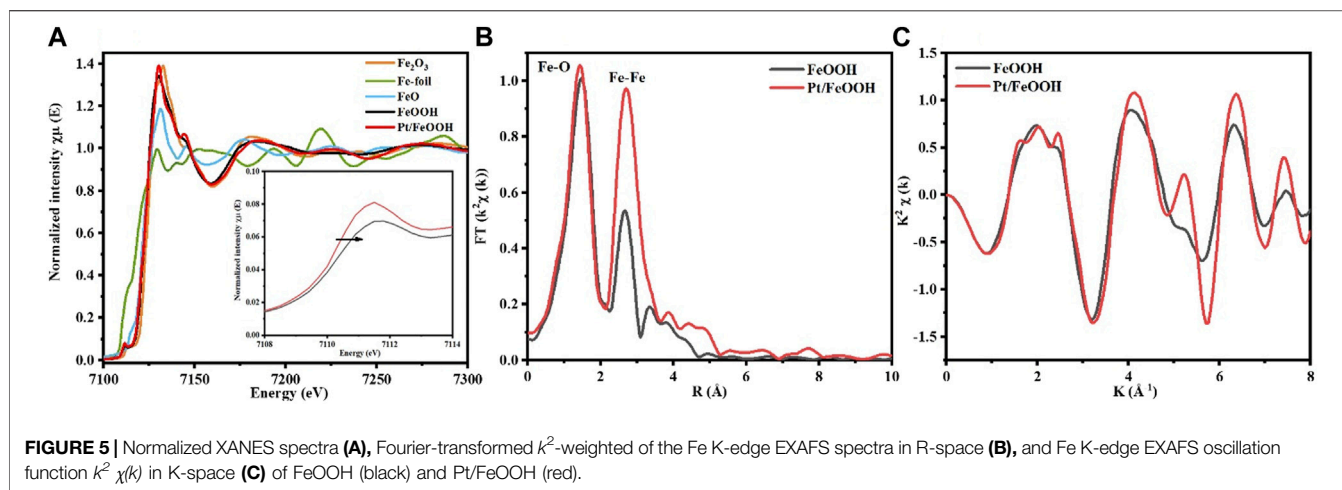
TABLE 3 | Fitted EXAFS results of Pt/FeOOH catalysts.

Sample	Shell	CN	R (Å)	σ^2 (Å^2)	E_o (eV)	R-factor
Fe-foil	Fe-Fe$_1$	8	2.47	0.0044	-0.7	0.003
	Fe-Fe$_2$	6	2.85	0.0057	-0.7	
Fe$_2$O$_3$	Fe-O	6	1.99	0.0137	3.2	0.008
	Fe-Fe$_1$	4	2.97	0.0075	7.8	
	Fe-Fe$_2$	3	3.39	0.0075	7.8	
	Fe-Fe$_3$	6	3.70	0.0075	7.8	
FeO	Fe-O	6	2.18	0.0039	9.9	0.014
	Fe-Fe	12	3.02	0.0134	-2.0	
FeOOH	Fe-O	5.6	1.98	0.0125	-1.1	0.001
	Fe-Fe$_1$	10.0	3.13	0.0225	8.0	
	Fe-Fe$_2$	7.8	3.47	0.0225	8.0	
Pt/FeOOH	Fe-O	6.0	1.94	0.013	-2.8	0.001
	Fe-Fe$_1$	9.7	3.18	0.0174	6.9	
	Fe-Fe$_2$	6.4	3.53	0.0174	6.9	

FIGURE 6 | H$_2$-TPR profiles of FeOOH and Pt/FeOOH.
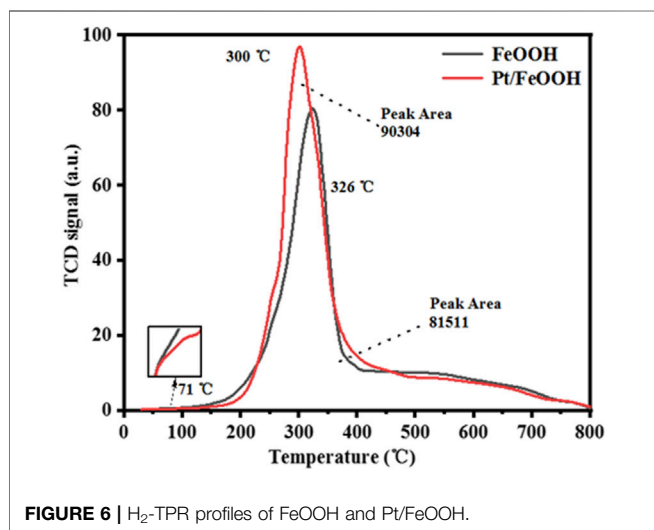
signals remained weak because the mass fraction for Pt was too low. But for the Pt/FeOOH, a broad peak appears at ~3.0 Å which indicates the existence of Pt-O-Fe coordination in the

second shell (Liu et al., 2018; Ren et al., 2019; Sadykov et al., 2021).

Redox Properties

As is often reported, the catalytic activity of the photocatalyst or thermalcatalyst is intimately associated with the reducibility of catalysts, especially at low temperatures. Hydrogen temperature-programmed reduction (H$_2$-TPR) is a powerful tool to determine the reducibility of the catalyst. The H$_2$-TPR profiles of FeOOH and Pt/FeOOH are shown in **Figure 6**.

The TPR profiles of the two samples show dominant H$_2$ consumption peaks at 300–326°C with shoulders extending to 800°C, ascribing to the surface oxygen and lattice oxygen, respectively. The H$_2$ consumption peak of Pt/FeOOH at 300°C is much lower than that of FeOOH (326°C), indicating that the interaction between Pt and FeOOH leads to more active interfaces. More intense H$_2$ consumption of FeOOH at the light-off temperature (71°C) can be ascribed to the higher adsorbed oxygen species due to the defect-rich surface of FeOOH QDs. It is noticeable that the H$_2$-TPR peaks of FeOOH QDs locate at a much lower temperature than those in references [385°C (Fan et al., 2017)], indicating that FeOOH QDs have better redox properties than larger FeOOH particles.

Optical Properties and Radical Characterizations

The UV-visible diffuse reflection spectroscopy (UV-vis DRS) was used to determine the light responses of samples, and the results are shown in **Figure 7A**. Both FeOOH and Pt/FeOOH can respond to a wide light region of 200–700 nm, showing good UV light and visible light absorbance. Loading Pt improves the light absorbance of FeOOH to some extent but does not dominate the optical property of the catalyst. The calculated parameters of energy bands of FeOOH and Pt/FeOOH are summarized in **Supplementary Table S1**. Pt/FeOOH shows a reduced bandgap (1.97 eV) compared with that of pristine FeOOH (2.02 eV). **Figure 7B** shows the photoluminescence (PL) spectra of both samples. The peak intensity of FeOOH is
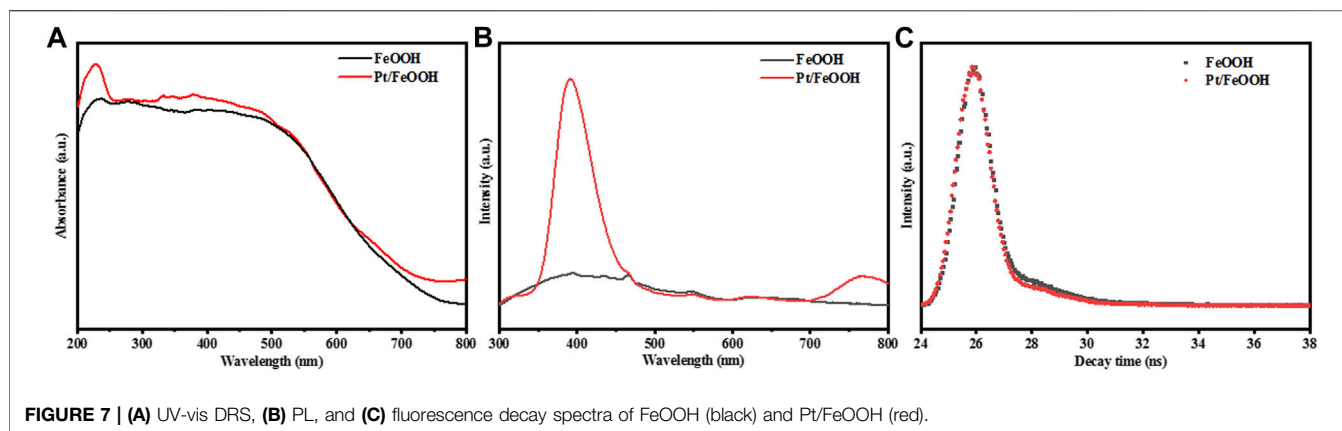
FIGURE 7 | (A) UV-vis DRS, **(B)** PL, and **(C)** fluorescence decay spectra of FeOOH (black) and Pt/FeOOH (red).
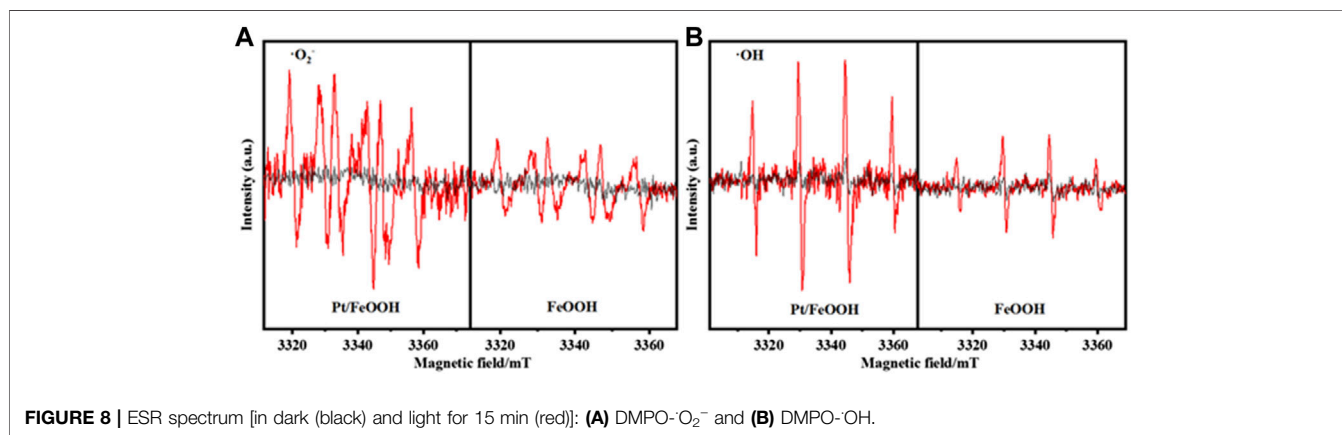
FIGURE 8 | ESR spectrum [in dark (black) and light for 15 min (red)]: **(A)** DMPO-·O_2^- and **(B)** DMPO-·OH.

lower than that of Pt/FeOOH in the whole wavelength, which means more electron-hole generate on Pt/FeOOH. Interestingly, the PL spectrum of Pt/FeOOH shows an extremely intense peak at 400 nm and a larger peak area than that of FeOOH which means a strong light response. Usually, the increase in the PL intensity means low separation efficiency. But from **Figure 7C**, the fluorescence decay of samples suggests that there is no obvious difference in the apparent lifetimes of charges on FeOOH and Pt/FeOOH, which means a short charge transmission path in Pt/FeOOH improves the photogenerated electron-hole separation efficiency due to its QD properties and optical properties.

Electron spin resonance (ESR) spectra are used to analyze the radicals of ●O_2^- and ●OH on the surface of catalysts under visible light irradiation. The generation of ●O_2^- is ascribed to the reduction of O_2 *via* the capture of conduction-band electrons: $O_2 + e^- \rightarrow$ ●O_2^-, while the ●OH radicals are generated *via* hydroxyls activated by holes (h$^+$): $OH^- + h^+ \rightarrow$ ●OH (Qian et al., 2019). As is displayed in **Figure 8**, Pt/FeOOH shows more intense signals of radicals under the light irradiation for 15 min than FeOOH, indicating higher electron-hole utilization efficiency for Pt/FeOOH. Thus, combining the results of XPS, H_2-TPR, UV-vis, PL, and ESR, Pt/FeOOH shows exceedingly strong oxygen activation ability and can utilize the electron and
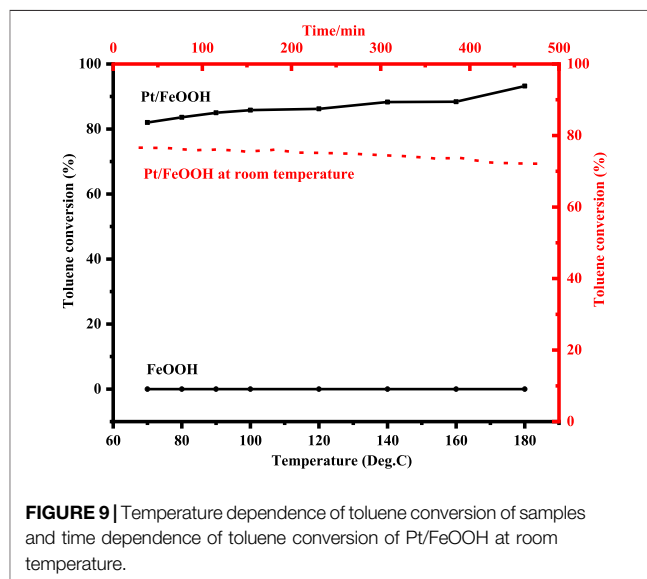
FIGURE 9 | Temperature dependence of toluene conversion of samples and time dependence of toluene conversion of Pt/FeOOH at room temperature.

hole more efficiently to generate radicals. On the other hand, the oxygen will be activated immediately as soon as the electrons and holes generate and then participate in the reactions, resulting in a high degradation efficiency of toluene oxidation.

FIGURE 10 | ORR polarization curves of Pt/C and Pt-FeOOH under oxygen-saturated 0.1 M KOH solution at a scan rate of 10 mV/s.
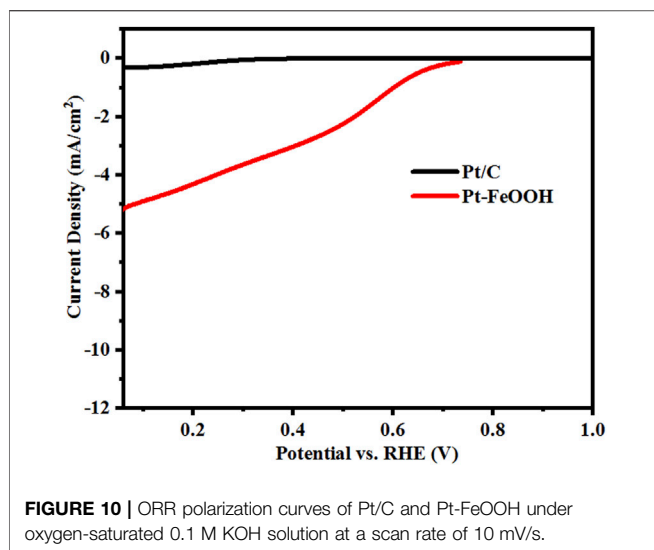
Photocatalytic Toluene Oxidation Performance

The photocatalytic performances of FeOOH and Pt/FeOOH in toluene oxidation are shown in **Figure 9**, and the control experiments are shown in **Supplementary Figure S9**. The pristine FeOOH shows no toluene degradation even at 180°C, while after the loading of sub-nano Pt, Pt/FeOOH shows 77% of

toluene conversion at room temperature, and the conversion slightly increases with the elevation in temperature, reaching 93.2% at 180°C, suggesting that the toluene oxidations are mainly from the photocatalysis. It is indicated that with the participation of Pt, O_2 molecules and hydroxyl groups are activated easily, and the toluene oxidation reaction can proceed efficiently. Furthermore, Pt/FeOOH maintains excellent stability (toluene conversion of 74.2%) at room temperature for 480 min. It should be mentioned that in this work, the weight hourly space velocity (WHSV) = 23,340 ml/(g h) is high enough to exclude the external diffusion influence and present the true activity of the catalyst. Meanwhile, the apparent activation energy E_a of Pt/FeOOH is only 1.34 kJ/mol (shown in **Supplementary Figure S6**), which is marvelously lower than our previous results, 56.7 kJ/mol of the Pd/CeO$_2$ catalyst (Zou et al., 2016) and 13.85 kJ/mol of Pd/CeO$_2$/Ag catalysts (Gao et al., 2019), indicating the metal–support interface may be essential for the toluene oxidation reaction.

The transition-metal-oxide/noble-metal interfaces are considered as the active sites for O_2 dissociation (Fu et al., 2010; Fu et al., 2013), and the Fe-O bilayer was considered to be the most active site in PROX, and excess H_2 helped stabilize the active structure (Fu et al., 2013). Differently, in this work, it is proposed that Pt nanoparticles can activate the lattice oxygen of FeOOH quantum dots support *via* forming Pt-O-Fe bonds in the second shell of β-FeOOH (EXAFS result), and the weakened Fe-O-H bonds will create more active radicals (such as OH) for

FIGURE 11 | Schematic representation of the photocatalysis mechanism .
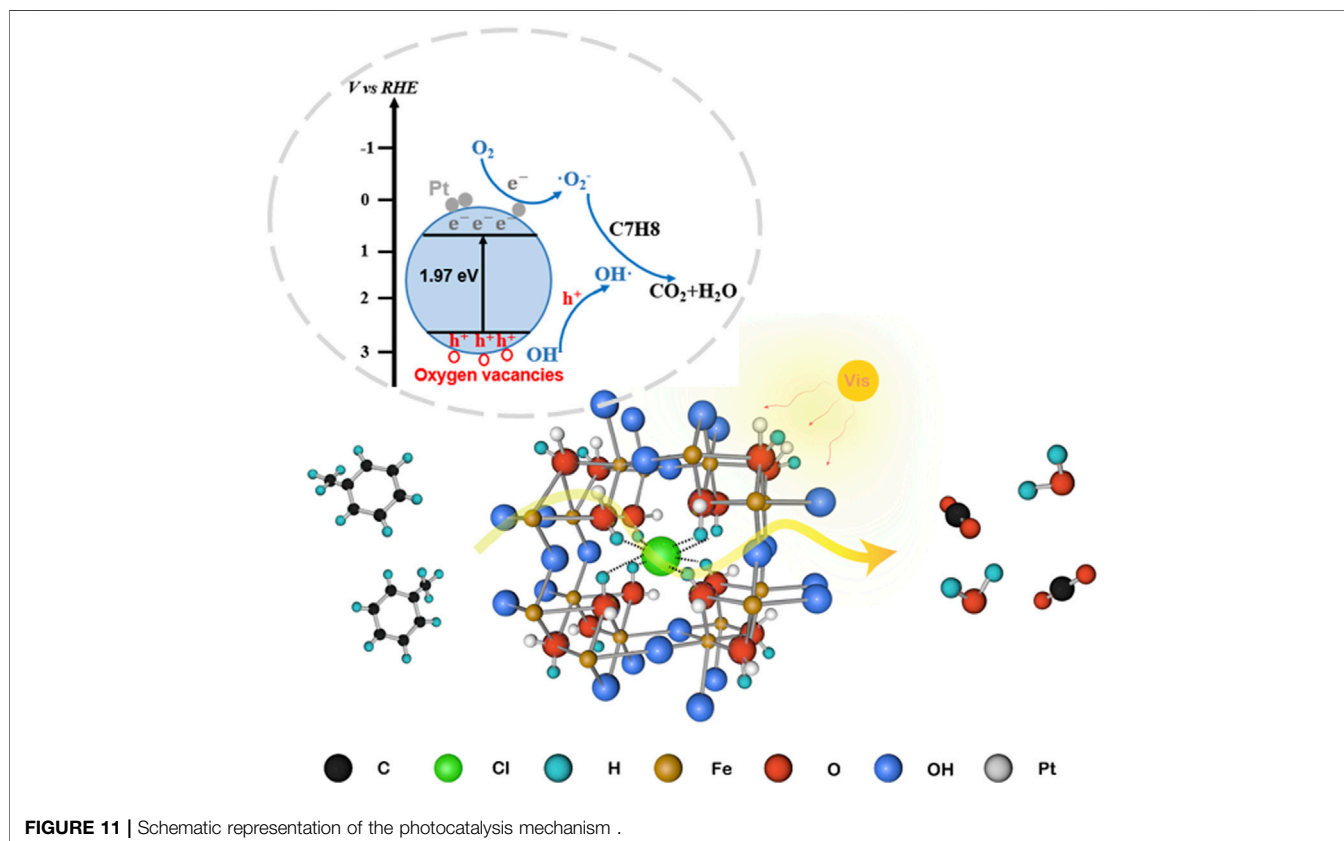
toluene oxidation. It is noteworthy that the wide light responses, good crystallization, and small sizes of FeOOH QDs benefit the charge generation and transfer to the surface species on the catalyst. Thus, the toluene oxidation can be accelerated through the Mars–van Krevelen reaction mechanism. Moreover, it is generally believed that the metallic Pt^0 is an active catalytic center for the activation of the C-H bond of toluene, which is also crucial to starting the reaction of toluene oxidation (Yuan et al., 2014). In order to verify the role of interfaces for O_2 activation, the catalytic performances of Pt/ FeOOH (with Pt-V_O-Fe interfaces) and Pt/C (without Pt-V_O-Fe interfaces) with the same Pt content (0.2%) in O_2 reduction reactions (ORR) were characterized (shown in **Figure 10**). The Pt/FeOOH sample presents a significantly higher current density under the same potential than Pt/C, consolidating that Pt/ FeOOH with Pt-V_O-Fe-rich interfaces has more active sites for the activation of O_2. Therefore, based on the aforementioned results, the photocatalysis mechanism schematic representation is shown in **Figure 11**.

CONCLUSION

In this work, a novel Pt/FeOOH QDs catalyst is prepared for efficient photocatalytic toluene oxidation. The loading of sub-nanometer-sized Pt atoms plays a key role in the crystallization of FeOOH QDs that H_2 spillover on Pt facilitates the release of H_2O and then improves the reconstruction of QDs. The interplay of Pt and FeOOH improves the kinetics of the photocatalytic reactions by activating surface oxygen. Due to the aforementioned advantages, the Pt/FeOOH catalyst exhibits an excellent catalytic activity, showing the toluene conversion of 74.2% after 8 h reaction at room temperature under visible light irradiation. Furthermore, the nano-scale catalyst offers an opportunity for matching the time scale and spatial scale in photocatalytic reactions. The study provides a new design strategy for photocatalysts.

EXPERIMENTAL SECTION

Chemicals and Materials

$FeCl_3.6H_2O$ (AR, 99 wt%) was purchased from Shanghai Macklin Biochemical Co., Ltd. NH_4HCO_3 (AR), and $H_2PtCl_6.6H_2O$ (AR, Pt ≥ 37.5 wt%) was purchased from Shanghai Aladdin Biochemical Technology Co., Ltd. All the chemical materials were used directly without any purification.

Catalyst Preparation

FeOOH QDs were synthesized by the liquid precipitation method *via* a facile chemical reaction between ferric chloride and precipitants. For the typical synthesis, 1 mmol of $FeCl_3.6H_2O$ was dissolved in 50 ml of absolute alcohol and ultrasound treated for 0.5 h. Then, 3 mmol of NH_4HCO_3 was added to the mixture with magnetic stirring at room temperature (Yang et al., 2018). After 12 h of magnetic stirring, products were collected by centrifugation and

washed several times with alcohol and deionized water and then dried in a vacuum oven at 60°C.

Pt/FeOOH quantum dots (Pt/FeOOH) were synthesized *via* a simple impregnation reduction method. FeOOH QDs were well-dispersed in deionized water with magnetic stirring and ultrasound treatment. Then, $H_2PtCl_6.6H_2O$ was added to the colloidal solution drop by drop, and the mixture was stirred for half an hour. After that, $NaBH_4$ solution was added to the mixture under magnetic stirring for another half an hour. Products were collected according to the same way as FeOOH QDs. The Pt/ amorphous FeOOH QDs were synthesized *via* the same impregnation reduction method except for replacing the $NaBH_4$ solution with methanol. Crystalline β-FeOOH QDs were synthesized *via* a simple hydrothermal method with $FeCl_3.6H_2O$, NH_4HCO_3, and ethanol at 120°C. The digital images of the main samples are shown in **Supplementary Figure S1**. The real Pt-loading contents of the main samples were analyzed by inductively coupled plasma spectrometry–atomic emission spectrometry (ICP-AES), and the results are shown in **Table 2**.

Catalyst Characterization

The crystalline properties of the catalyst were analyzed by X-ray diffraction (XRD, Bruker D8) using Cu $K_α$ ($λ$ = 1.5406 Å) radiation. The specific surface area and pore structure of catalysts were analyzed by the Brunauer–Emmett–Teller (BET) technique using the ASAP 2020M + C surface area analyzer by N_2 adsorption. The metal concentration of Pt was determined by ICP-AES (Varian 720-ES). Atomic force microscopy (AFM, Bruker Dimension Icon) and special aberration-corrected transmission electron microscopy (AC STEM, FEI Titan Cubed Themis G2 300) were used to detect the microstructure and morphology of the catalysts. Raman spectra (Raman, HORIBA JY LabRAM HR800), Fourier transform infrared spectroscopy (FT-IR, PerkinElmer Spectrum 100 with a resolution of 4 cm^{-1}), X-ray photoelectron spectroscopy (XPS, PHI 5000 VersaProbe II with monochromatic Al $K_α$ radiation), and extended X-ray absorption fine structure (EXAFS, BSRF, Beijing, China) were used to analyze the chemical and element coordination environment. UV-vis diffuse reflectance spectroscopy (UV-vis DRS, SHIMADZU UV-2450 with $BaSO_4$ as the internal standard), ultraviolet photoelectron spectroscopy (UPS, ESCALAB 250Xi, 2 × 10^{-8} mbar, 21.22 eV, 16 mA), and photoluminescence (PL, HORIBA FluoroMax-4) spectrum were used to analyze the optical properties. Hydrogen-temperature–programmed reduction (H_2-TPR, 10°C/min, from 30 to 900°C in a flow of 10% H_2-90% Ar (v/v) mixture) was used to detect the redox properties. The electron spin resonance (ESR, Bruker E500, 100 mM DMPO, 50 mM TEMP, 200 μM TEMPO, •O_2^- in methanol and •OH in water, sample concentration is 0.1 mg/ml) was used to detect active radicals. The electrochemical measurement for ORR was performed by using a rotating disk electrode (area: 0.196 cm^2) connected to an installation of rotating electrode speed control. The Hg_2SO_4 electrode was used as the reference electrode, and

the Pt electrode was used as the counter electrode in 0.1 M KOH solutions. The scan and rotation rates for ORR measurements were 10 mV/s and 1600 r.p.m, respectively.

Photocatalytic Toluene Degradation

The degradation of toluene was evaluated in a stainless steel continuous flow reactor with a quartz glass window (inner diameter = 20 mm). A 150–300 W Xenon lamp source (CEL-HXF300) equipped with a UV-vis filter (λ = 400–800 nm) was placed above the reactor.

Before the catalytic evaluation test, 100 mg of the catalyst was well-dispersed on quartz wool and placed in an aluminum foil, and then, they were placed on the bottom of the reaction tube. The surface temperature of the catalyst was detected by a thermocouple put in the center of the catalyst layer. For the test of toluene oxidation, the reaction mixture gas was 2080 ppm toluene + N_2 (balance gas), and the total flow rate was 38.9 ml/min [sccm, corresponding to the weight hourly space velocity (WHSV) = 23,340 ml/(gh)]. The change in the reactant concentration in catalytic oxidation of toluene was monitored by using a gas chromatograph (GC). The toluene conversion was calculated by using the following equation:

$$\text{Toluene conversion (\%)} = 100\% \times \big(\,[\text{Toluene}]_{\text{inlet}}$$
$$- [\text{Toluene}]_{\text{outlet}}\big)/\,[\text{Toluene}]_{\text{inlet}}, \quad (1)$$

Where $[\text{Toluene}]_{\text{inlet}}$ and $[\text{Toluene}]_{\text{outlet}}$ represent the inlet and outlet toluene concentrations through GC.

TOF_{Pt} was calculated according to the following equation:

$$\text{TOF}_{\text{Pt}}\,(s^{-1})\,\frac{\text{toluene concentration on stream }\left(\frac{\text{mol}}{\text{mol}}\right)\times}{22.4\times\left(\frac{\text{mol}}{\text{L}}\right)\times 60\times 1000\times \text{Pt sites}\left(\frac{1}{\text{mol}}\right)}. \quad (2)$$

DATA AVAILABILITY STATEMENT

The original contributions presented in the study are included in the article/**Supplementary Material**; further inquiries can be directed to the corresponding author.

AUTHOR CONTRIBUTIONS

MP: prepared and characterized the catalysts and wrote part of the manuscript. ZS: designed the whole research plan and initiated this project. YL and SL: wrote part of this manuscript. XW and RR: modified the manuscript. DW: helped in the characterization of catalysts and modified the manuscript. FK: helped in the characterization of catalysts and modified the manuscript.

SUPPLEMENTARY MATERIAL

The Supplementary Material for this article can be found online at: https://www.frontiersin.org/articles/10.3389/fmats.2022.846376/full#supplementary-material

REFERENCES

Asahi, R., Morikawa, T., Ohwaki, T., Aoki, K., and Taga, Y. (2001). Visible-Light Photocatalysis in Nitrogen-Doped Titanium Oxides. *Science* 293, 269–271. doi:10.1126/science.1061051

Chen, Y.-Z., Wang, Z. U., Wang, H., Lu, J., Yu, S.-H., and Jiang, H.-L. (2017). Singlet Oxygen-Engaged Selective Photo-Oxidation over Pt Nanocrystals/Porphyrinic MOF: The Roles of Photothermal Effect and Pt Electronic State. *J. Am. Chem. Soc.* 139 (5), 2035–2044. doi:10.1021/jacs.6b12074

Dong, Y., Wang, X., Fu, Q., and Pan, C. (2021). Construction of Direct Z-Scheme Heterojunction NiFe-Layered Double Hydroxide (LDH)/$Zn_{0.5}Cd_{0.5}S$ for Photocatalytic H_2 Evolution. *ACS Appl. Mat. Interfaces* 13 (33), 39331–39340. doi:10.1021/acsami.1c09650

Duan, M., Yu, J., Meng, J., Zhu, B., Wang, Y., and Gao, Y. (2018). Reconstruction of Supported Metal Nanoparticles in Reaction Conditions. *Angew. Chem. Int. Ed.* 57, 6464–6469. doi:10.1002/anie.201800925

Einaga, H., Ogata, A., Futamura, S., and Ibusuki, T. (2001). The Stabilization of Active Oxygen Species by Pt Supported on TiO_2. *Chem. Phys. Lett.* 338, 303–307. doi:10.1016/s0009-2614(01)00296-2

Fan, H., Huang, X., Kähler, K., Folke, J., Girgsdies, F., Teschner, D., et al. (2017). *In-Situ* Formation of Fe Nanoparticles from FeOOH Nanosheets on γ-Al_2O_3 as Efficient Catalysts for Ammonia Synthesis. *ACS Sustain. Chem. Eng.* 5, 10900–10909. doi:10.1021/acssuschemeng.7b02812

Fu, Q., Li, W.-X., Yao, Y., Liu, H., Su, H.-Y., Ma, D., et al. (2010). Interface-Confined Ferrous Centers for Catalytic Oxidation. *Science* 328, 1141–1144. doi:10.1126/science.1188267

Fu, Q., Yang, F., and Bao, X. (2013). Interface-Confined Oxide Nanostructures for Catalytic Oxidation Reactions. *Acc. Chem. Res.* 46, 1692–1701. doi:10.1021/ar300249b

Gao, J., Si, Z., Xu, Y., Liu, L., Zhang, Y., Wu, X., et al. (2019). Pd-Ag@CeO_2 Catalyst of Core-Shell Structure for Low Temperature Oxidation of Toluene Under Visible Light Irradiation. *J. Phys. Chem. C* 123, 1761–1769. doi:10.1021/acs.jpcc.8b09060

Guo, Y., Wen, M., Li, G., and An, T. (2021). Recent Advances in VOC Elimination by Catalytic Oxidation Technology onto Various Nanoparticles Catalysts: a Critical Review. *Appl. Catal. B Environ.* 281, 119447. doi:10.1016/j.apcatb.2020.119447

Gurbani, N., Han, C.-P., Marumoto, K., Liu, R.-S., Choudhary, R., Choudhary, R. J., et al. (2018). Biogenic Reduction of Graphene Oxide: An Efficient Superparamagnetic Material for Photocatalytic Hydrogen Production. *ACS Appl. Energy Mat.* 1 (44), 5907–5918. doi:10.1021/acsaem.8b00552

Han, T., Cao, X., Sun, K., Peng, Q., Ye, C., Huang, A., et al. (2021). Anion-Exchange-Mediated Internal Electric Field for Boosting Photogenerated Carrier Separation and Utilization. *Nat. Commun.* 12, 4952. doi:10.1038/s41467-021-25261-8

Hosseini, S. M., Ghiaci, M., Kulinich, S. A., Wunderlich, W., Farrokhpour, H., Saraji, M., et al. (2018). Au-Pd@g-C_3N_4 as an Efficient Photocatalyst for Visible-Light Oxidation of Benzene to Phenol: Experimental and Mechanistic Study. *J. Phys. Chem. C* 122, 27477–27485. doi:10.1021/acs.jpcc.8b08788

Hu, J., Li, S., Chu, J., Niu, S., Wang, J, Du, Y., et al. (2019). Understanding the Phase-Induced Electrocatalytic Oxygen Evolution Reaction Activity on FeOOH Nanostructures. *ACS Catal.* 9 (12), 10705–10711. doi:10.1021/acscatal.9b03876

Huang, J., He, S., Goodsell, J. L., Mulcahy, J. R., Guo, W., Angerhofer, A., et al. (2020). Manipulating Atomic Structures at the Au/TiO_2 Interface for O_2 Activation. *J. Am. Chem. Soc.* 142 (14), 6456–6460. doi:10.1021/jacs.9b13453

Jouyandeh, M., Soroush, S., Khadem, M., Habibzadeh, S., Esmaeili, A., Abida, O., et al. (2021). Quantum Dots for Photocatalysis: Synthesis and Environmental Applications. *Green Chem.* 23 (2021), 4931–4954. doi:10.1039/D1GC00639H

Kang, L., Liu, X. Y., Wang, A., Li, L., Ren, Y., Li, X., et al. (2020). Photo-Thermo Catalytic Oxidation over a TiO_2 -WO_3 -Supported Platinum Catalyst. *Angew. Chem. Int. Ed.* 59, 12909–12916. doi:10.1002/anie.202001701

Liu, L., Yang, L. Q., Liang, H. W., Cong, H. P., Jiang, J., and Yu, S. H. (2013). Bio-inspired Fabrication of Hierarchical FeOOH Nanostructure Array Films at the Air-Water Interface, Their Hydrophobicity and Application for Water Treatment. *Acs Nano* 7 (7), 1368–1378. doi:10.1021/nn305001r

Liu, J., Zheng, M., Shi, X., Zeng, H., and Xia, H. (2016). Amorphous FeOOH Quantum Dots Assembled Mesoporous Film Anchored on Graphene Nanosheets with Superior Electrochemical Performance for Supercapacitors. *Adv. Funct. Mat.* 26, 919–930. doi:10.1002/adfm.201504019

Liu, R., Ma, L., Niu, G., Li, X., Li, E., Bai, Y., et al. (2017). Flexible Ti-Doped FeOOH Quantum Dots/Graphene/Bacterial Cellulose Anode for High-Energy Asymmetric Supercapacitors. *Part. Part. Syst. Charact.* 10 (34), 1700213. doi:10.1002/ppsc.201700213

Liu, B., Wang, Y., Peng, H. Q., Yang, R., Jiang, Z., Zhou, X., et al. (2018). Iron Vacancies Induced Bifunctionality in Ultrathin Feroxyhyte Nanosheets for Overall Water Splitting. *Adv. Mater* 30, e1803144. doi:10.1002/adma.201803144

Mamaghani, A., Haghighat, F., and Lee, C. (2017). Photocatalytic Oxidation Technology for Indoor Environment Air Purification: The State-Of-The-Art. *Appl. Catal. B Environ.* 203, 247–269. doi:10.1016/j.apcatb.2016.10.037

Marsh, A. L., Burnett, D. J., Fischer, D. A., Gland, J. L., and John, L. (2004). *In-Situ* Soft X-Ray Studies of Toluene Catalytic Oxidation on the Pt(111) Surface. *J. Phys. Chem. B* 108, 605–611. doi:10.1021/jp0353035

Mateo, D., Cerrillo, J. L., Durini, S., and Gascon, J. (2021). Fundamentals and Applications of Photo-Thermal Catalysis. *Chem. Soc. Rev.* 50, 2173–2210. doi:10.1039/d0cs00357c

Mi, R., Li, D., Hu, Z., and Yang, R. T. (2021). Morphology Effects of CeO_2 Nanomaterials on the Catalytic Combustion of Toluene: A Combined Kinetics and Diffuse Reflectance Infrared Fourier Transform Spectroscopy Study. *ACS Catal.* 11, 7876–7889. doi:10.1021/acscatal.1c01981

Niklas, S., Alexander, L., Zalibera, M., Frenzel, J., Daniel, M. S., Savitsky, A., et al. (2018). Atomic Scale Explanation of O_2 Activation at the Au-TiO_2 Interface. *J. Am. Chem. Soc.* 140 (51), 18082–18092. doi:10.1021/jacs.8b10929

Pal, R., Wang, L.-M., Pei, Y., Wang, L.-S., and Zeng, X. C. (2012). Unraveling the Mechanisms of O_2 Activation by Size-Selected Gold Clusters: Transition from Superoxo to Peroxo Chemisorption. *J. Am. Chem. Soc.* 134 (22), 9438–9445. doi:10.1021/ja302902p

Peng, L., Yang, N., Yang, Y., Wang, Q., Xie, X., Sun-Waterhouse, D., et al. (2021). Atomic Cation-Vacancy Engineering of NiFe-Layered Double Hydroxides for Improved Activity and Stability towards the Oxygen Evolution Reaction. *Angew. Chem.* 133 (46), 24817–24824. doi:10.1002/ange.202109938

Qian, R., Zong, H., Schneider, J., Zhou, G., Zhao, T., Li, Y., et al. (2019). Charge Carrier Trapping, Recombination and Transfer during TiO_2 Photocatalysis: An Overview. *Catal. Today* 335 (335), 78–90. doi:10.1016/j.cattod.2018.10.053

Ren, Y., Tang, Y., Zhang, L., Liu, X., Li, L., Miao, S., et al. (2019). Unraveling the Coordination Structure-Performance Relationship in $Pt1/Fe_2O_3$ Single-Atom Catalyst. *Nat. Commun.* 10, 4500. doi:10.1038/s41467-019-12459-0

Sadykov, I. I., Zabilskiy, M., Clark, A. H., Krumeich, F., Sushkevich, V., van Bokhoven, J. A., et al. (2021). Time-Resolved XAS Provides Direct Evidence for Oxygen Activation on Cationic Iron in a Bimetallic Pt-$FeOx/Al_2O_3$ Catalyst. *ACS Catal.* 11 (18), 11793–11805. doi:10.1021/acscatal.1c02795

Sakamoto, H., Ohara, T., Yasumoto, N., Shiraishi, Y., Ichikawa, S., Tanaka, S., et al. (2015). Hot-Electron-Induced Highly Efficient O_2 Activation by Pt Nanoparticles Supported on Ta_2O_5 Driven by Visible Light. *J. Am. Chem. Soc.* 137 (29), 9324–9332. doi:10.1021/jacs.5b04062

Schreck, M., and Niederberger, M. (2019). Photocatalytic Gas Phase Reactions. *Chem. Mat.* 31 (3), 597–618. doi:10.1021/acs.chemmater.8b04444

Song, X., and Boily, J.-F. (2012). Structural Controls on OH Site Availability and Reactivity at Iron Oxyhydroxide Particle Surfaces. *Phys. Chem. Chem. Phys.* 14, 2579–2586. doi:10.1039/c2cp22715k

Song, X., and Boily, J.-F. (2016). Surface and Bulk Thermal Dehydroxylation of FeOOH Polymorphs. *J. Phys. Chem. A* 120, 6249–6257. doi:10.1021/acs.jpca.6b04294

van Deelen, T. W., Carlos Hernández, M., Hernández Mejía, C., and de Jong, K. P. (2019). Control of Metal-Support Interactions in Heterogeneous Catalysts to Enhance Activity and Selectivity. *Nat. Catal.* 2, 955–970. doi:10.1038/s41929-019-0364-x

Wang, H., Jiang, S., Shao, W., Zhang, X., Chen, S., Sun, X., et al. (2018). Optically Switchable Photocatalysis in Ultrathin Black Phosphorus Nanosheets. *J. Am. Chem. Soc.* 140 (9), 3474–3480. doi:10.1021/jacs.8b00719

Yang, Y.F, Liu, W., Wang, K., Li, W., and Li, J. (2018). Facile Synthesis of FeOOH Quantum Dots Modified ZnO Nanorods Films *via* a Metal-Solating Process. *ACS Sustain. Chem. Eng.* 6 (6), 7789–7798. doi:10.1021/acssuschemeng.8b00776

Yuan, T., Lai, T. C. C., Yi, K., Lan, B. S., Chen, J., You, C., et al. (2014). Pt/SBA-15 as a Highly Efficient Catalyst for Catalytic Toluene Oxidation. *ACS Catal.* 11 (4), 3824–3836. doi:10.1021/cs500733j

Zhong, Y., Peng, C., He, Z., Chen, D., Jia, H., Zhang, J., et al. (2021). Interface Engineering of Heterojunction Photocatalysts Based on 1D Nanomaterials. *Catal. Sci. Technol.* 11, 27–42. doi:10.1039/d0cy01847c

Zou, Z., Si, Z., Cao, Y., Ran, R., Wu, X., and Weng, D. (2016). Localized Surface Plasmon Resonance Assisted Photo-Thermal Catalysis of CO and Toluene Oxidation over Pd-CeO_2 Catalyst under Visible Light Irradiation. *J. Phys. Chem.C* 51 (120), 29116–29125. doi:10.1021/acs.jpcc.6b08630